CMS Physics Analysis Summary

Contact: cms-pag-conveners-exotica@cern.ch 2024/07/23

Search for t-channel scalar and vector leptoquark exchange in the high mass dimuon and dielectron spectrum in proton-proton collisions at $\sqrt{s} = 13$ TeV

The CMS Collaboration

Abstract

A search for t-channel exchange of leptoquarks (LQs) is performed using proton-proton collision data collected at $\sqrt{s} = 13$ TeV with the CMS detector at the CERN LHC. The data correspond to an integrated luminosity of 138 fb^{-1}. The search spans scenarios with scalar and vector LQs that couple up and down quarks to electrons and muons. Dielectron and dimuon final states are considered, with dilepton invariant masses above 500 GeV. The differential distributions of dilepton events are fit to templates built from reweighted samples of simulated standard model events. This method is able to probe higher LQ masses than previous pair-production and single-production searches. Limits are set on LQ-fermion coupling strengths for LQ masses up to 5 TeV. Based on the results, scalar LQs are excluded for masses up to 5 TeV for a coupling strength of 1.2, and vector LQs are excluded for masses up to 5 TeV for a coupling strength of 1.5.

1 Introduction

Leptoquarks (LQs) are hypothetical particles proposed to explore the similarities between the quark and lepton sectors of the standard model (SM). Leptoquarks were initially proposed in early extensions of the SM, such as Grand Unified theories based on $SU(5)$ and $SU(10)$ [1–5] like the Pati–Salam model, composite models [6, 7], and technicolor models [8–10]. They have also been proposed as mediators of interactions between the SM and dark matter [11, 12], and appear in R-parity violating supersymmetry models [13]. Recent results from the Muon $g-2$ experiment show deviations in the experimental value of the anomalous magnetic moment of the muon, at the level of 4.2σ [14], though the deviation is reduced when updated lattice quantum chromodynamics (QCD) calculations are considered [15]. A massive LQ could contribute to the anomalous magnetic moment by mixing with the SM Higgs field [16].

Leptoquarks are electrically charged, color-triplet bosons, either scalar or vector, that carry baryon number as well as lepton number. They carry fermion number $F = 3B + L$ of 0 or -2; however, $F = -2$ LQs can mediate proton decay, and stringent limits from dedicated proton decay searches have strongly constrained such LQs. Distinctions between different LQs are based on their SM gauge group transformation properties, giving rise to twelve LQ multiplets [17]. Only six families do not mediate proton decay. Leptoquarks are labelled as first-, second-, third-, or mixed-generation based on the SM quarks and leptons with which they interact.

The quark-LQ-lepton interaction is characterised by the LQ-fermion coupling constants, y_{LQ} for the scalar case and g_{LQ} for the vector case. In colliders, LQs can be produced singly or in pairs, or manifest via t-channel exchange. The pair-production channel is dominated by gluon-gluon fusion, with cross section proportional to the square of the strong coupling (α_s^2). Since this production mode proceeds via the strong interaction, it is insensitive to the LQ-fermion coupling, and is responsible for the most stringent bounds at lower LQ masses (m_{LQ}). The single-production cross section scales as $\alpha_s y_{\mathrm{LQ}}^2$, but the channel can be more sensitive than pair production at high m_{LQ} or y_{LQ}. Finally, the t-channel exchange process, shown in Fig. 1, has a cross section proportional to y_{LQ}^4, with additional contributions proportional to y_{LQ}^2 from the interference with dilepton production via the Drell-Yan (DY) process. This channel can have superior sensitivity at very high m_{LQ}, as its cross section decreases more slowly as a function of m_{LQ}.

Several searches for LQs have been performed by the ATLAS and CMS Collaborations. Leptoquarks coupling to τb were studied in Ref. [18], targeting single and pair production as well as t-channel LQ exchange. Leptoquarks with masses below 1.22–1.88 TeV were excluded for LQ-b-τ coupling values below 2.5, while an excess with a local significance of 2.8σ was observed for $m_{\mathrm{LQ}} = 2$ TeV and $y_{\mathrm{LQ}} = 2.5$. The t-channel exchange process is the most sensitive channel at large m_{LQ} and y_{LQ}, excluding LQs with masses up to 2.3 TeV for $y_{\mathrm{LQ}} = 3.5$. Vector LQs in $\tau\tau$ final states were studied in Ref. [19]. Limits were set on m_{LQ} as a function of g_{LQ} for two benchmark scenarios for the right-handed τb coupling matrix. Leptoquark masses of 1–5 TeV were excluded for all g_{LQ} greater than 1.3 (0.8) - 5.6 (3.2) for the first (second) benchmark scenario. The ATLAS Collaboration excluded LQs coupling to τb with $m_{\mathrm{LQ}} < 1.49$–1.96 TeV in the pair-production channel [20], as well as placing coupling-dependent limits on the single production and t-channel exchange of such LQs, up to 1.53(2.05) TeV for scalar (vector) LQs with $y_{\mathrm{LQ}} = 2.5$ [21]. For LQs coupling to first- and second-generation fermions, the most stringent limits have been set by ATLAS, excluding LQs with masses below 1.8 TeV and 1.7 TeV, respectively, independent of g_{LQ} and assuming a branching fraction of 100% [22]. Single production of first- and second-generation scalar LQs has been studied by CMS [23], in which LQs with masses below 1.73 TeV and 530 GeV respectively were excluded, assuming $g_{\mathrm{LQ}} = 1$ and a branching fraction of 100%. Pair production of first- and second-generation scalar LQs have also been studied by CMS [24, 25]. First generation scalar LQ masses were excluded up to 1.44 TeV, and second generation scalar LQ masses were excluded up to 1.53 TeV, independent of g_{LQ} and assuming a branching fraction of 100%.

This note presents the first search for the t-channel exchange of LQs coupling to first- and second-generation SM fermions, probing scalar and vector LQs with masses in the range 1–5 TeV. The search uses proton-proton (pp) collision data at $\sqrt{s} = 13$ TeV corresponding to an integrated luminosity of 138 fb^{-1}, collected by the CMS experiment at the CERN LHC in 2016–2018. The hypothetical signal process results in the nonresonant production of electron or muon pairs. It is distinguished from the dominant background of SM DY events using the differential distributions of the dilepton invariant mass, the angle between the incoming quark and the outgoing lepton, and the rapidity of the dilepton system. The observed dilepton distributions are fit with a combination of signal and background templates, both produced by reweighting SM DY Monte Carlo (MC) events. Following the notation of Ref. [26], three families of LQs are considered: two scalar doublet families, R_2 and $\widetilde{R}_2$, and one vector triplet family, U_3. The subscripts refer to the dimensionality of the $SU(2)$ representation. Within the R_2, $\widetilde{R}_2$, and U_3 families, we search for first-generation and mixed-generation LQs that couple up and down quarks to electrons and muons. For the scalar doublet families, following Ref. [26], we consider the case where the LQ couples only to right-handed quark multiplets and left-handed lepton multiplets (RL). The LQs are assumed to couple to a single quark and lepton, resulting in four scalar LQ coupling scenarios: two R_2 LQs, $\mathrm{S_{eu}}$ and $\mathrm{S_{\mu u}}$, and two $\widetilde{R}_2$ LQs, $\mathrm{S_{ed}}$ and $\mathrm{S_{\mu d}}$, where the subscripts denote the SM fermions. Similarly, four U_3 vector LQs are considered: $\mathrm{V_{eu}}$, $\mathrm{V_{\mu u}}$, $\mathrm{V_{ed}}$, and $\mathrm{V_{\mu d}}$. The SM gauge group transformation properties for the chosen LQ models are summarized in Table 1. A more detailed review of LQ physics in precision experiments can be found in Ref. [17]. The R_2 LQs appear in potential solutions to the muon anomalous magnetic moment problem [27], and U_3 LQs appear in models that describe scenarios for lepton flavour violation [28].

Table 1: Properties of the R_2, $\widetilde{R}_2$, and U_3 LQs. Specifically, this analysis searches for R_2 LQs with RL couplings and charge 5/3, $\widetilde{R}_2$ LQs with RL couplings and charge 2/3, and U_3 LQs with charges 2/3 and 5/3.

LQ family	$(SU(3), SU(2), U(1))$	Spin	Charge
R_2	(3, 2, 7/6)	0	5/3, 2/3
$\widetilde{R}_2$	(3, 2, 1/6)	0	2/3, −1/3
U_3	(3, 3, 2/3)	1	5/3, 2/3 −1/3

The LQ-quark-lepton interactions are defined by the following terms in the Lagrangian:

$$\mathcal{L} \supset g_{\ell \mathrm{u}} \bar{\mathrm{u}}_L \gamma^\mu \ell_L U_\mu^{5/3} + g_{\ell \mathrm{d}} \bar{\mathrm{d}}_L \gamma^\mu \ell_L U_\mu^{2/3} + y_{\ell \mathrm{u}} \bar{\mathrm{u}}_R \ell_L R^{5/3} + y_{\ell \mathrm{d}} \bar{\mathrm{d}}_R \ell_L \tilde{R}^{2/3} + \text{h.c.}, \tag{1}$$

where $g_{\ell u}$ ($g_{\ell d}$) are the vector couplings of the charge 5/3 (2/3) vector U_3 LQs to fermions and $y_{\ell u}$ ($y_{\ell d}$) are the scalar couplings of the charge 5/3 (2/3) R_2 ($\tilde{R}_2$) scalar LQs to fermions.

2 Analysis strategy

The t-channel LQ exchange occurs in conjunction with the SM DY process, which is the primary background for this search. This analysis utilizes three variables computed from the dilepton

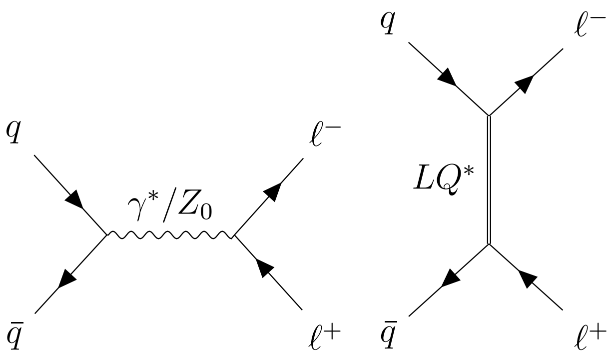

Figure 1: Leading order diagrams for SM DY production (left) and t-channel LQ exchange (right). The LQ amplitude interferes with the Z/γ^* amplitude.

system: the invariant mass, $m_{\ell\ell}$; the rapidity y; and $\cos\theta^*$ (abbreviated as c_*), the cosine of the angle between the quark (as opposed to the antiquark) and the lepton in the Collins-Soper frame [29, 30]. At a pp collider, the direction of the incident quark is unknown, so we instead define an approximation, $\cos\theta_R \equiv \frac{p_z}{|p_z|} c_*$ (abbreviated as c_R), which uses the fact that the quark will typically have higher longitudinal momentum than the antiquark, and hence the longitudinal momentum of the dilepton system will more often align with that of the quark. The observed distributions in these three variables can be expressed as a convolution of the underlying differential cross section:

$$f(m^r_{\ell\ell}, y^r, c_R) = C \int \mathrm{d}m_{\ell\ell}\, \mathrm{d}y\, \mathrm{d}c_* R(m^r_{\ell\ell}, y^r, c_R; m_{\ell\ell}, y, c_*) \varepsilon(m_{\ell\ell}, y, c_*) \frac{\mathrm{d}^3\sigma}{\mathrm{d}m_{\ell\ell}\, \mathrm{d}y\, \mathrm{d}c_*} \qquad (2)$$

where the superscript r distinguishes reconstructed variables from generator-level variables, C is a normalization constant, R is a resolution function that incorporates detector resolution and parton shower effects, and ε is an efficiency function. Since the convolution is a linear function of the cross section, σ, the resulting reconstructed distribution can be expressed as a sum of convolutions of different contributions to the total cross section. The linearity allows the expected observation for a given signal hypothesis to be represented as a sum of templates that are individually independent of the parameters of interest. Specifically, the parton-level differential cross section of the SM DY process can be written as:

$$\left[\frac{\mathrm{d}\sigma}{\mathrm{d}c_*}(m^2_{\ell\ell})\right]_{\mathrm{DY}} \propto \frac{3}{8}\left\{(1+c_*^2) + A_4 c_* + \frac{A_0}{2}\left(1-3c_*^2\right)\right\}, \qquad (3)$$

where A_4 and A_0 are the standard dimensionless coefficients parametrizing the angular distribution of the DY process [31, 32]. This form of the angular distribution is general for any spin-1, s-channel process. The first two terms correspond to the leading order (LO) in QCD, and the third term corresponds to next-to-LO (NLO). The coefficients A_0 and A_4 are functions of $m_{\ell\ell}$, the transverse momentum (p_T) and y of the dilepton system. Measurements of A_0 probe higher-order corrections in perturbative QCD, whereas A_4 is directly related to the SM forward-backward asymmetry, $A_{FB} = (\sigma_F - \sigma_B)/(\sigma_F + \sigma_B) = \frac{3}{8}A_4$, where σ_F and σ_B are the cross sections for forward ($c_* > 0$) and backward ($c_* < 0$) events, respectively.

The leading-order doubly differential cross section for t-channel exchange of a scalar LQ can be expressed as [26],

$$\frac{\mathrm{d}^2\sigma}{\mathrm{d}m_{\ell\ell}\mathrm{d}c_*} \propto \left[\frac{\mathrm{d}^2\sigma}{\mathrm{d}m_{\ell\ell}\mathrm{d}c_*}\right]_{\mathrm{DY}} + y^4_{\mathrm{LQ}} N^S_{\mathrm{LQ(pure)}}(m_{\ell\ell}) \left(\frac{1-c_*}{1-c_*+\frac{2m^2_{\mathrm{LQ}}}{m^2_{\ell\ell}}}\right)^2 + y^2_{\mathrm{LQ}} N^S_{\mathrm{LQ(int)}}(m_{\ell\ell}) \left[\frac{(1-c_*)^2}{1-c_*+\frac{2m^2_{\mathrm{LQ}}}{m^2}}\right], \quad (4)$$

and the differential cross section for a vector LQ exchange can be expressed as,

$$\frac{\mathrm{d}^2\sigma}{\mathrm{d}m_{\ell\ell}\mathrm{d}c_*} \propto \left[\frac{\mathrm{d}^2\sigma}{\mathrm{d}m_{\ell\ell}\mathrm{d}c_*}\right]_{\mathrm{DY}} + g^4_{\mathrm{LQ}} N^V_{\mathrm{LQ(pure)}}(m_{\ell\ell}) \left(\frac{1+c_*}{1-c_*+\frac{2m^2_{\mathrm{LQ}}}{m^2_{\ell\ell}}}\right)^2 + g^2_{\mathrm{LQ}} N^V_{\mathrm{LQ(int)}}(m_{\ell\ell}) \left[\frac{(1+c_*)^2}{1-c_*+\frac{2m^2_{\mathrm{LQ}}}{m^2_{\ell\ell}}}\right] \quad (5)$$

where $N^{S,V}_{\mathrm{LQ(pure)}}$ and $N^{S,V}_{\mathrm{LQ(int)}}$ are functions of $m_{\ell\ell}$. The first LQ-specific term corresponds to pure t-channel LQ exchange, while the second term corresponds to the interference of the t-channel LQ exchange with the SM Z/γ^* diagram.

Following a similar approach to that in Ref. [30], the templates are histograms binned in three variables ($m_{\ell\ell}$, c_{R}, and y), constructed from simulated SM DY events that are reweighted using functions of the generator-level variables to represent each of the terms in Eqs. (4) or (5). A maximum likelihood fit of a linear combination of the templates to the observed data is performed to extract the signal and background parameters, namely A_0, A_4, and either y_{LQ} or g_{LQ}. The template construction is described in more detail in Section 7. Each of the eight combinations of spin and coupling to SM fermions is probed separately.

3 The CMS detector and event reconstruction

The central feature of the CMS apparatus is a superconducting solenoid of 6 m internal diameter, providing a magnetic field of 3.8 T. Within the solenoid volume are a silicon pixel and strip tracker, a lead tungstate crystal electromagnetic calorimeter (ECAL), and a brass and scintillator hadron calorimeter (HCAL), each composed of a barrel and two endcap sections. Forward calorimeters extend the pseudorapidity coverage provided by the barrel and endcap detectors. Muons are detected in gas-ionization chambers embedded in the steel flux-return yoke outside the solenoid. A more detailed description of the CMS detector, together with a definition of the coordinate system used and the relevant kinematic variables, is reported in Ref. [33, 34].

Events of interest are selected using a two-tiered trigger system. The first level, composed of custom hardware processors, uses information from the calorimeters and muon detectors to select events at a rate of around 100 kHz within a fixed latency of about 4 μs [35]. The second level, known as the high-level trigger (HLT), consists of a farm of processors running a version of the full event reconstruction software optimized for fast processing, and reduces the event rate to around 1 kHz before data storage [36].

A particle-flow algorithm [37] aims to reconstruct and identify each individual particle in an event, with an optimized combination of information from the various elements of the CMS detector. The energy of photons is obtained from the ECAL measurement. The energy of electrons is determined from a combination of the electron momentum at the primary interaction vertex as determined by the tracker, the energy of the corresponding ECAL cluster, and the energy sum of all bremsstrahlung photons spatially compatible with originating from the electron track. The energy of muons is obtained from the curvature of the corresponding track. The energy of charged hadrons is determined from a combination of their momentum measured in the tracker and the matching ECAL and HCAL energy deposits, corrected for the response function of the calorimeters to hadronic showers. Finally, the energy of neutral hadrons is obtained from the corresponding corrected ECAL and HCAL energies. The primary vertex is taken to be the vertex corresponding to the hardest scattering in the event, evaluated using tracking information alone, as described in Section 9.4.1 of Ref. [38].

Muons are measured in the range $|\eta| < 2.4$, with detection planes made using three technologies: drift tubes, cathode strip chambers, and resistive-plate chambers. The single-muon trigger efficiency exceeds 90% over the full η range, and the efficiency to reconstruct and identify muons is greater than 96%. Matching muons to tracks measured in the silicon tracker results in a relative p_{T} resolution of 1% in the barrel and 3% in the endcaps for muons with p_{T} up to 100 GeV, and of better than 7% for muons in the barrel with p_{T} up to 1 TeV [39].

The single-electron trigger efficiency is approximately 80% over the full η range, and the efficiency to reconstruct and identify electrons is greater than 65% for electrons with $p_{\mathrm{T}} > 20$ GeV. The momentum resolution for electrons with $p_{\mathrm{T}} \approx 45$ GeV from $\mathrm{Z} \to \mathrm{ee}$ decays ranges from 1.7–4.5%. It is generally better in the barrel region than in the endcaps, and also depends on the bremsstrahlung energy emitted by the electron as it traverses the material in front of the ECAL [40].

For each event, hadronic jets are clustered from these reconstructed particles using the infrared and collinear safe anti-k_{T} algorithm [41, 42] with a distance parameter of 0.4. Jet momentum is determined as the vectorial sum of all particle momenta in the jet, and is found from simulation to be, on average, within 5–10% of the true momentum over the whole p_{T} spectrum and detector acceptance. Additional pp interactions within the same or nearby bunch crossings (pileup) can contribute additional tracks and calorimetric energy depositions, increasing the apparent jet momentum. To mitigate this effect, tracks identified as originating from pileup vertices are discarded and an offset correction is applied to correct for remaining contributions [43]. Jet energy corrections are derived from simulation studies so that the average measured energy of jets becomes identical to that of particle level jets [44]. In situ measurements of the momentum balance in dijet, photon+jet, Z+jet, and QCD multijet events are used to determine any residual differences between the jet energy scale in data and in simulation, and appropriate corrections are made [44]. The missing transverse momentum vector ($\vec{p}_{\mathrm{T}}^{\mathrm{miss}}$) is defined as the negative vector p_{T} sum of all the particle-flow candidates in an event, and its magnitude is denoted as $p_{\mathrm{T}}^{\mathrm{miss}}$ [45]. The $\vec{p}_{\mathrm{T}}^{\mathrm{miss}}$ is modified to account for corrections to the energy scale of the reconstructed jets in the event.

4 Simulated event samples

Various MC event generators are used to simulate the SM background processes. The DY samples are generated at NLO in QCD with up to two extra partons using MADGRAPH5_aMC@NLO [46] v2.2.2 (v2.6.0) for samples corresponding to the 2016 (2017–2018) data-taking period. The parton shower, hadronization, and quantum electrodynamics final-state radiation are simulated with PYTHIA v8.226 (v8.230) [47], using the FXFX merging scheme and parton shower tune CUETP8M1 (CP5). The NLO NNPDF 3.0 parton distribution functions (PDFs) [48, 49] are used for all three data-taking periods.

Additional backgrounds include diboson production (WW, WZ, ZZ), photon-induced dilepton production ($\gamma\gamma \to \ell\ell$), top quark pair production ($t\bar{t}$), and single top quark production in association with a W boson (tW). The $t\bar{t}$ and tW backgrounds are generated at NLO using POWHEG v2.0 [50–53], and interfaced to PYTHIA with the CUETP8M2T4 [54] (CP5) tune for the 2016 (2017–2018) data-taking period. The diboson background samples are generated at NLO, with ZZ $\to \ell\ell\ell'\ell'$, ZZ $\to \ell\ell\nu\nu$, and WW $\to \ell\nu\ell\nu$ processes generated using POWHEG and WZ $\to$ qq$\ell\ell$, WZ $\to \ell\ell\ell\nu$ and ZZ $\to$ qq$\ell\ell$ processes generated using MADGRAPH5_aMC@NLO. All diboson samples are showered using PYTHIA and tune CUETP8M1 (CP5) for the 2016 (2017–2018) data-taking periods. The $t\bar{t}$, tW, and diboson backgrounds use the NNPDF 3.0 (3.1) PDFs for 2016 (2017–2018) data-taking periods. The photon-induced background, $\gamma\gamma \to \ell\ell$, is simulated using the CEPGEN [55] implementation of LPAIR [56, 57], interfaced to PYTHIA v6.429 [58], using the Suri-Yennie proton structure function parametrization [59]. This contribution is split into three parts because the interaction at each proton vertex can be elastic or inelastic.

The cross sections for the WZ and ZZ samples are normalized to the NLO predictions calculated with MCFM 6.6 [60], while the cross sections of the WW samples are normalized to the next-to-NLO (NNLO) predictions [61]. The total cross section for the $t\bar{t}$ process is normalized to the prediction with NNLO accuracy in QCD and next-to-next-to-leading-logarithmic accuracy for the soft gluon radiation resummation calculated with TOP++ 2.0 [62].

Leptoquark signal samples are generated using the SLQrules package [63]. These samples are used only for cross checks on the LQ template method.

The detector response for all MC samples is simulated using GEANT4 [64]. The pileup distribution in simulation is weighted to match the one observed in data.

5 Event selection

Events are required to have two leptons of the same flavor and opposite charges. The dimuon and dielectron events are selected by single-muon and single-electron triggers, respectively. The leading muon and electron p_T requirement for all three years is 40 GeV. The subleading lepton is required to have $p_T > 15$ GeV. The events selected by the triggers are reconstructed and required to satisfy a number of offline requirements. All muons are required to be within the acceptance of the muon system ($|\eta| < 2.4$), and all electrons must be within $|\eta| < 2.5$, excluding the barrel-endcap transition region of the ECAL ($1.44 < |\eta| < 1.57$). Additionally, to remove cosmic ray-induced events, the azimuthal angle (ϕ) between the two muons is required to differ from π by more than 5 mrad.

Each reconstructed muon is required to pass identification criteria that are based on the number of hits observed in the tracker, the response of the muon detectors, and a set of matching criteria between muon track parameters, as measured by the inner tracker and muon detectors. To suppress nonprompt muons coming from heavy-flavor decays, both muons must be isolated from other particles in a cone of size $\Delta R = 0.3$, where $\Delta R = \sqrt{(\Delta\eta)^2 + (\Delta\phi)^2}$ refers to the distance from the muon to a given track. More details on the muon identification and reconstruction used in this analysis can be found in Refs. [39, 65].

The reconstructed electron candidates are required to pass identification criteria that are based on electromagnetic shower shape variables. Electrons originating from photon conversions are suppressed by requiring that the candidates have at most one missing inner tracker hit and not be consistent with being part of a conversion pair. Electrons are also required to be isolated from other particles within a cone of size $\Delta R = 0.3$. The electron isolation criteria are based on the ratio of the electron p_T to the sum of energy deposits associated with the photons as well as with the charged and neutral hadrons reconstructed by the particle-flow algorithm. More details on the electron reconstruction and identification criteria used in this analysis are described in Ref. [40].

Events in the signal region must have $m_{\ell\ell} > 500$ GeV. We do not apply any selection criteria based on p_T^{miss}, nor do we veto events containing b-tagged jets. In Ref. [30], which considered events with $m_{\ell\ell} > 170$ GeV, these cuts were applied to suppress backgrounds that contain the decays of top quarks; in this analysis, such backgrounds are suppressed by the $m_{\ell\ell} > 500$ GeV requirement. Moreover, we retain sensitivity to some LQ scenarios producing b jets in the final state, as predicted by some models that could explain lepton flavour universality violation using mixed-generation LQs [66].

6 Backgrounds

The dominant background comes from DY events, and the subdominant background consists of fully leptonic decays of $t\bar{t}$ events. Backgrounds from tW events, diboson processes and $\tau\tau$ leptonic decays are also included. All of these backgrounds are well modeled in simulation. The estimated event yields of the $t\bar{t}$, tW, $\tau\tau$ and diboson backgrounds are validated in data in a control region of eμ events.

An additional background arises from events where one or more jets are incorrectly identified as leptons, primarily W+jets events and events composed uniquely of jets produced through the strong interaction, referred to as QCD multijet events. Such events are referred to as MisID events. This background is larger for the ee channel than for the $\mu\mu$ channel. A technique based on control samples in data is employed to estimate this background. A small fraction of the background comes from t-channel photon-induced dilepton production, which is modeled with MC simulation as well. For the dimuon (dielectron) channel, the background consists of approximately 85% (82%) DY, 10% (9%) $t\bar{t}$, 5% (4%) diboson, and 0.5% (5%) MisID events.

The MisID background is estimated from data using the "misidentification rate" method [67, 68]. The misidentification rate is defined as the probability of a jet, having been reconstructed as a lepton candidate, to pass the lepton selection requirements. This rate is measured in a sample with two reconstructed leptons from a Z boson decay and an additional, potentially misidentified lepton. The two leptons corresponding to a Z decay are required to pass the lepton identification requirements and have an invariant mass within 7 GeV of the Z boson mass [69]. The third lepton candidate is used as a probe to measure the misidentification rate. This third lepton candidate is required to pass a less stringent set of identification and isolation requirements than the full selection requirements of the analysis. The MisID background can then be estimated from control samples of data events with two lepton candidates: one sample in which one lepton fails the full selection requirements which would model the W+jets events, and another sample in which both leptons fail the requirements, whch would model the QCD multijet events. Events from this sample are assigned weights based on the expected misidentification probability of the failing lepton candidates. Contamination of this sample by lepton pairs from DY and other prompt processes is subtracted using MC simulation. These reweighted events are used to estimate the yield and shape of the MisID background.

The MisID background estimation is validated in a control region with the same selection criteria as the signal region, except the lepton pairs are required to have same-sign rather than opposite-sign charges. A large fraction of the events in this control region stem from misidentified jets. In the ee channel, there is a significant contribution to this sample from opposite-sign

DY events where the charge of one of the electrons has been incorrectly assigned. The rate of charge misassignment in simulation is corrected using a sample of dilepton events near the Z peak with $70 < m_{\ell\ell} < 110$ GeV. The MisID background estimate as well as MC estimates of other backgrounds are compared with the observed yield of same-sign events. A c_R-dependent correction to the MisID background estimate is derived using the ratio of the MisID estimate to the number of observed same-sign events minus other backgrounds. The uncertainty in this correction is calculated as the quadratic sum of the statistical uncertainties from the limited sample size, uncertainty in the number of DY pairs reconstructed as same-sign pairs, as well as a systematic uncertainty reflecting possible differences in shape between same-sign and opposite-sign MisID estimates.

The $\tau\tau$, tW, $t\bar{t}$, and diboson backgrounds are validated in data using eμ events. The eμ control region has the same selection criteria as the signal region, except that events are required to have one muon and one electron rather than a pair of the same flavor. The muon is required to have $p_T > 40$ GeV and pass the single-muon trigger, and the electron is required to have $p_T > 15$ GeV. The MisID background is also present in this eμ control region and is estimated using the misidentification rate technique previously described. Good agreement is observed between the simulated and observed yield of eμ events across the entire mass range.

Because diboson events are produced via electroweak processes, they are expected to have a small forward-backward asymmetry in their lepton pairs; $t\bar{t}$ events are also known to have an asymmetry, but it is too small to be detected using leptons alone [70]. The QCD and W+jets backgrounds are expected to have no asymmetry. Based on MC and control sample estimates, we predict an overall forward-backward asymmetry of $A_{FB} \approx 0.01$ in the sample of eμ events. The observed value in the eμ control sample is $A_{FB} = 0.012 \pm 0.003$, consistent with this expectation.

Although the overall normalizations and asymmetries in eμ events are observed to be consistent between data and simulation, there are discrepancies between the predicted and observed shapes of the c_R distribution. To address these discrepancies, a correction is derived from the ratio of the c_R distributions in data and simulation in eμ events, and applied to the shape of the c_R distributions in simulation. Because the asymmetry is modeled well, this correction is derived symmetrically in c_R using four bins of $|c_R|$. A single correction is derived in the 500–3000 GeV mass range because of the limited event count. This correction modifies the shapes of the templates used to model the corresponding backgrounds in the signal region by 5–25%. The statistical uncertainty in each of the four $|c_R|$ bins is modeled as a separate shape nuisance.

Figure 2 shows a comparison between measured $\mu\mu$ and ee events and the background prediction in the signal region after all corrections have been applied. Good agreement is observed between the simulated and observed number of $\mu\mu$ and ee events.

7 Template construction

To model the dilepton differential distributions, we construct parameter-independent templates for each piece of the differential cross section of LQ production shown in Eqs. (4) and (5). For the SM DY component, the differential cross section is reparametrized as follows:

$$\left[\frac{d\sigma}{dc_*}(m_{\ell\ell}^2)\right]_{DY} \propto \frac{3}{4(2+\alpha)}\left\{(1+c_*^2) + \frac{(2+\alpha)}{2}\, A_4\, c_* + \alpha(1-c_*^2)\right\}, \qquad (6)$$

where $\alpha = \frac{2A_0}{2-A_0}$. The first two terms are symmetric and antisymmetric in c_*, respectively, and

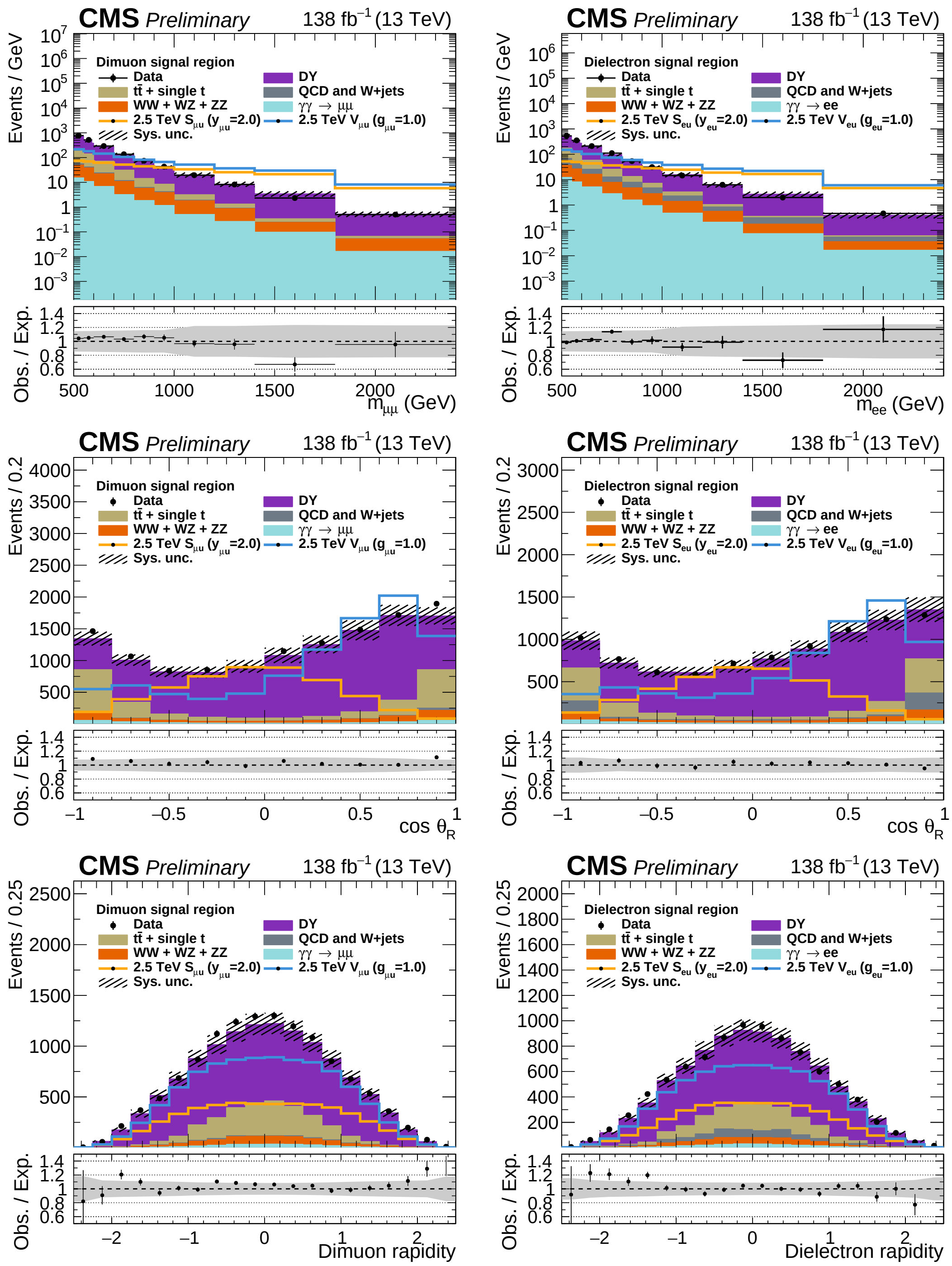

Figure 2: A comparison of data and expected background distributions in dilepton invariant mass (upper row), c_R (middle row) and dilepton rapidity (lower row). The left (right) plots show the $\mu\mu$ (ee) channel. The blue histogram represents the signal yield of a hypothetical 2.5 TeV S_{eu} ($S_{\mu u}$) with $y_{eu}(y_{\mu u}) = 2.0$, while the yellow histogram represents the signal yield of a hypothetical 2.5 TeV $V_{eu}(V_{\mu u})$ with $g_{eu}(g_{\mu u}) = 1.0$. The black points with error bars represent the data and their statistical uncertainties. The background expectation is shown as stacked histograms. The hatched band shows the total systematic uncertainty in the expected background yield. The lower panels show the ratio of the data to the expectation. The gray bands represents the normalized uncertainty in the predicted yield. The error bars in the ratio plot represent the normalized statistical uncertainty of the data.

the third term is proportional to α. The LQ exchange comprises two terms with coefficients y_{LQ}^4 or g_{LQ}^4 for the pure exchange of the LQ and y_{LQ}^2 or g_{LQ}^2 for the interference with Z/γ^*. We denote the templates for these five pieces of the cross section as f_{s}, f_{a}, and f_α for the three DY templates and $f_{\text{LQ(pure)}}$ and $f_{\text{LQ(int)}}$ for the pure and interference LQ terms.

In Ref. [30], the f_{s}, f_{a}, and f_α templates are constructed by binning events in c_{R} and $|y|$. We extend these two dimensional templates to three dimensions by additionally binning in reconstructed dilepton mass. The templates are constructed by reweighting simulated DY events as analytical functions of generator-level quantities to match the differential distributions of the three pieces of the DY cross section. To reduce statistical fluctuations in the MC, each event is used twice, once with $+c_*$ and once with $-c_*$, with a weight of 0.5 to keep the normalization unchanged. The reweighting functions for the DY templates, f_{a}, f_{s}, and f_α respectively are:

$$w_{\text{a}}(c_*) = \frac{c_*}{1 + c_*^2 + \alpha\,(1 - c_*^2)} \tag{7}$$

$$w_{\text{s}}(|c_*|) = \frac{1 + c_*^2}{1 + c_*^2 + \alpha\,(1 - c_*^2)} \tag{8}$$

$$w_\alpha(|c_*|) = \frac{1 - c_*^2}{1 + c_*^2 + \alpha\,(1 - c_*^2)}. \tag{9}$$

The denominator of the DY reweighting functions is extracted for each event by looking up the bin contents of simulated DY events that are binned in $\cos\theta^*$ and generator-level $|y|$. The α values in the denominator are determined by fitting the generator-level distributions of the simulated events. Finally, to avoid negative values in the antisymmetric template, f_{a}, a linear combination of f_{s} and f_{a} is used in the fit, defined by $f_\pm = \frac{f_{\text{s}} \pm f_{\text{a}}}{2}$.

For the templates corresponding to the two LQ terms, $f_{\text{LQ(pure)}}$ and $f_{\text{LQ(int)}}$, events are reweighted as functions of both c_* and $m_{\ell\ell}$. The reweighting functions are given by:

$$w^{S,V}_{\text{LQ(pure)}}(c_*, m_{\ell\ell}) = \left(N^{S,V}_{\text{LQ(pure)}}(m_{\ell\ell}) \frac{(1 \mp c_*)^2}{(1 - c_* + \frac{2m_{\text{LQ}}^2}{m_{\ell\ell}^2})^2} \right) \frac{1}{N_{\text{SM}}(m_{\ell\ell})(1 + c_*^2)} \tag{10}$$

$$w^{S,V}_{\text{LQ(int)}}(c_*, m_{\ell\ell}) = \left(N^{S,V}_{\text{LQ(int)}}(m_{\ell\ell}) \frac{(1 \mp c_*)^2}{(1 - c_* + \frac{2m_{\text{LQ}}^2}{m_{\ell\ell}^2})} \right) \frac{1}{N_{\text{SM}}(m_{\ell\ell})(1 + c_*^2)}, \tag{11}$$

where S and V denote the scalar or vector case. The prefactors, $N^{S,V}_{\text{LQ}}(m_{\ell\ell})$, depend on the vector and axial vector couplings of the quarks and leptons to the Z boson, as well as the charges of the quarks. Thus, templates for different LQs coupling different leptons and quarks have different shapes. The $N_{\text{SM}}(m_{\ell\ell})$ prefactor represents the coefficient of the symmetric term $(1 + c_*^2)$ in the SM DY angular distribution. Note that the denominators of the LQ reweighting functions are different from those of the SM DY functions, calculated from the analytical form of the LO SM DY cross section for each event. This is because the LQ modifies the dilepton mass distribution, which must be taken into account in the reweighting.

The reweighting procedure described above has several benefits. The effects of misassigning the direction of the incident quark in the c_* computation, called the "dilution" effect, are accounted for correctly. Additionally, no dedicated MC samples need to be produced for the LQ process or its interference. The distribution of LQ events can be obtained by reweighting SM DY MC events using the analytical functional form of the LQ differential cross section.

The total template for the scalar LQ case, binned in reconstructed $m_{\ell\ell}$, y, and c_{R} is given by:

$$f_{\mathrm{data}} = \sum_j f^j_{\mathrm{bk}} + N(\alpha)\left(\alpha\, f_\alpha + \left(1+\frac{3A_4}{8N}\right) f_+ + \left(1-\frac{3A_4}{8N}\right) f_-\right) + y^4_{\mathrm{LQ}} f_{\mathrm{LQ(pure)}} + y^2_{\mathrm{LQ}} f_{\mathrm{LQ(int)}}, \tag{12}$$

where f^j_{bk} are templates for the non-DY backgrounds and $N(\alpha) = \frac{3}{4(2+\alpha)}$. The same template is used for the vector LQ case using the corresponding reweighting functions, and replacing y_{LQ} with g_{LQ}. The coefficients A_4, α, and either y^2_{LQ} or g^2_{LQ} are extracted in the fits to data.

Events are divided into bins based on $m_{\ell\ell}$, $|y|$, and c_{R}. For $m_{\ell\ell}$, four bins are used with bin edges at 500, 700, and 1000 GeV, with the fourth bin containing all events with $m_{\ell\ell} > 1000$ GeV. Three bins are defined for $|y|$, with edges at 0, 0.6, 1, and 2.4. The binning in c_{R} depends on the rapidity. Within the first rapidity bin, events are divided into eight bins in c_{R} of width 0.25. For the other two rapidity bins, events are divided into six bins in c_{R}, with edges of -1, -0.5, -0.25, 0, 0.25, 0.5, and 1.

Additional templates are created for the other background processes, with one template each for the MisID background, photon-induced dilepton production, DY $\tau\tau$ production, the combined top quark backgrounds ($\mathrm{t\bar{t}}$, Wt), and the combined diboson backgrounds (WW, ZZ, WZ). The top quark and MisID templates are symmetrized in c_{R} to reduce statistical fluctuations (the top quark backgrounds do have a small inherent asymmetry, below the sensitivity of this analysis). The diboson, photon-induced dilepton, and DY $\tau\tau$ backgrounds are not symmetrized because of their significant inherent asymmetry.

8 Systematic uncertainties

Systematic uncertainties in the normalization and shapes of the templates arise from a variety of sources, and are incorporated in the fit to data through nuisance parameters in the likelihood. Systematic uncertainties affecting template normalizations are included using log-normal priors. For systematic uncertainties that change the shape of a template, shifted templates are constructed by varying the source of the systematic uncertainty up and down within its uncertainty. The uncertainties are incorporated into the likelihood by interpolation between the nominal and shifted templates, constrained with a Gaussian prior. Tables 2 and 3 shows the impact of each uncertainty on the fitted LQ coupling for representative scalar and vector signal hypotheses.

A significant source of uncertainty is due to the creation of the LQ signal templates using LO reweighting of NLO DY MC events. An uncertainty of 60% is assigned on the LQ interference template, and 120% on the LQ pure template. These uncertainties are based on bias tests performed on simulation with injected signal events that were generated using MADGRAPH5_aMC@NLO using Ref. [63].

Several sources of systematic uncertainty are due to the modeling of leptons in simulation. These include uncertainties in the momentum scale, the efficiency of the reconstruction and identification criteria, and the trigger efficiency. These uncertainties are small for the muon channel, but are the dominant uncertainty for the electron channel at high LQ masses, contributing up to 0.16–23% of the uncertainty on g^2_{LQ} or y^2_{LQ}.

Additional systematic uncertainties are applied to templates estimated from simulation. The uncertainty in the PDFs is assigned from the Hessian variations of the PDF sets. Uncertainties due to missing higher order contributions are estimated by varying the renormalization and factorization scales independently by factors of two. Additional uncertainties are assigned to the cross sections of the DY, $\mathrm{t\bar{t}}$, and diboson processes based on comparisons between generators, of size 3%, 5%, and 4%, respectively. Similarly, an uncertainty of 6% is assigned to the normalization of the $\gamma\gamma \to \ell\ell$ process, based on a comparison between the Suri-Yennie structure functions and the LuxQED photon PDFs [71, 72]. The statistical uncertainties due to the limited number of MC events is implemented using the simplified Barlow-Beeston approach [73]. Since the bin contents of $\pm c_*$ are correlated because each event is used twice, each pair of $\pm c_*$ bins is varied together and accounts for a separate nuisance.

The MisID background is assigned a normalization uncertainty of 50% based on closure studies of the misidentification rate in simulation, and a separate shape uncertainty based on the difference between the MisID estimate in same-sign and opposite-sign events. The MisID uncertainty primarily affects the electron channel, given the higher rate of misidentified electrons than muons.

The $\mathrm{t\bar{t}}$ and diboson templates are assigned a shape uncertainty due to the correction to the c_{R} distributions derived from $\mathrm{e}\mu$ events. The integrated luminosities for the 2016, 2017, and 2018 data-taking years have 1.2–2.5% individual uncertainties [74–76], while the overall uncertainty for the 2016–2018 period is 1.6%. Small uncertainties in the modeling of pileup are also incorporated.

In general, systematic uncertainties are found to be sub-dominant as compared to statistical ones, except for the vector LQs that couple to muons.

Table 2: The contribution of statistical uncertainty and individual sources of systematic uncertainty to the total variance on the fitted value of y^2_{LQ} for a scalar LQ mass of 2.5 TeV. For a given source of uncertainty, the impact is determined by fixing its associated nuisance parameter to the nominal expectation and evaluating the change in the total uncertainty.

Source	Contribution to uncertainty on y^2_{LQ} (%)			
	y^2_{eu}	y^2_{ed}	$y^2_{\mu\mathrm{u}}$	$y^2_{\mu\mathrm{d}}$
Statistical uncertainty	82	82	83	78
LQ LO reweighting	3.3	4.3	2.7	3.2
MC and MisID backgrounds statistical uncertainty	1.6	3.2	1.3	1.9
α_s + renormalization/factorization scales	0.5	0.7	2.9	4.0
$\mathrm{e}\mu$ shape corrections	0.6	0.6	1.4	1.1
Background cross sections	0.8	0.5	5.3	6.6
Luminosity & pileup	0.7	1.1	2.1	3.2
PDFs	$<$0.1	0.3	0.5	0.5
Trigger & prefire correction	0.8	0.6	0.1	$<$0.1
Momentum scale	3.6	4.7	0.1	$<$0.1
Identification/isolation	3.9	0.4	$<$0.1	0.7
MisID shape & normalization	2.1	4.1	1.4	1.9

Table 3: The contribution of statistical uncertainty and individual sources of systematic uncertainty to the total variance on the fitted value of g^2_{LQ} for a vector LQ mass of 2.5 TeV. For a given source of uncertainty, the impact is determined by fixing its associated nuisance parameter to the nominal expectation and evaluating the change in the total uncertainty.

Source	Contribution to uncertainty on g^2_{LQ} (%)			
	g^2_{eu}	g^2_{ed}	$g^2_{\mu\mathrm{u}}$	$g^2_{\mu\mathrm{d}}$
Statistical uncertainty	99	52	31	46
LQ LO reweighting	<0.1	4.1	20	10
MC and MisID backgrounds statistical uncertainty	<0.1	6.6	6.9	5.7
α_s + renormalization/factorization scales	<0.1	2.1	5.8	6.6
eμ shape corrections	<0.1	0.3	1.8	0.4
Background cross sections	<0.1	3.3	21	16
Luminosity & pileup	<0.1	3.3	7.4	10
PDFs	<0.1	0.5	0.9	0.9
Trigger & prefire correction	<0.1	0.5	0.1	0.3
Momentum scale	0.1	0.7	1.5	0.3
Identification/isolation	0.2	23	1.0	1.6
MisID shape & normalization	<0.1	8.6	7.0	6.0

9 Results

Template fits are performed to the data for each LQ signal hypothesis, following Eq. (12). The COMBINE package [77] is used to perform maximum likelihood fits to the data. The fit results are shown in Figs. 3–10. The extracted best fit parameters for a candidate LQ mass of 2.5 TeV are shown in Tables 4 and 5. All results are found to be consistent with SM background expectations. The uncertainties on the couplings are asymmetric due to the nature of the likelihood.

Limits at 95% confidence level (CL) are set on the absolute value of the LQ-fermion couplings as a function of the LQ mass for each coupling and spin hypothesis. The limit setting procedure uses a modified frequentist approach based on the $\mathrm{CL_s}$ criterion [78, 79] using an asymptotic approximation for the test statistic [80]. The limits are shown in Figs. 11 and 12 for the scalar case and Figs. 13 and 14 for the vector case, assuming branching fractions of 100% for each channel. In general, for equal coupling values, the cross sections for vector LQ production are larger than for scalar LQ production, hence the limits on g_{LQ} are generally stronger than those on y_{LQ}. The limits on up-type couplings are stronger than the limits on down-type couplings because of the larger up quark content of the PDFs. Additionally, the limits on LQs coupling to muons are slightly more stringent than LQs coupling to electrons because of more efficient selection criteria.

For the scalar case, coupling values of 0.4–1.1 (0.3–1.0) are excluded for LQs coupling to electrons (muons) with masses between 1–5 TeV. These limits significantly extend the previous best limits from single production [23], which excluded $\mathrm{S_{eu}}$ and $\mathrm{S_{ed}}$ masses upto 1.7 TeV depending on the coupling, and pair production [24], which excluded $\mathrm{S_{eu}}$ and $\mathrm{S_{ed}}$ masses upto 1.4 TeV independent of the mass. Similarly, for the vector case, couplings values of 0.2–0.5 (0.1–0.4) are excluded for LQs coupling to electrons (muons). These are the first limits set on vector LQs coupling to first- and second-generation fermions.

10 Summary

A search for the t-channel exchange of leptoquarks (LQs) coupling to first- and second-generation fermions has been presented. The search uses proton-proton collision data at $\sqrt{s} = 13$ TeV, cor-

Table 4: Best fit values of A_0, A_4 and y^2_{LQ} for scalar LQ models. Results are shown for a candidate m_{LQ} of 2.5 TeV.

Model	A_0	A_4	y^2_{LQ}
S_{eu}	0.07 ± 0.07	1.61 ± 0.08	$-0.10^{+0.15}_{-0.17}$ (stat)$^{+0.07}_{-0.11}$ (syst)
S_{ed}	0.07 ± 0.07	1.62 ± 0.08	$-0.09^{+0.20}_{-0.23}$ (stat)$^{+0.11}_{-0.13}$ (syst)
$S_{\mu u}$	0.02 ± 0.06	1.59 ± 0.07	$-0.13^{+0.14}_{-0.15}$ (stat)$^{+0.06}_{-0.11}$ (syst)
$S_{\mu d}$	0.02 ± 0.06	1.60 ± 0.07	$-0.11^{+0.18}_{-0.20}$ (stat)$^{+0.09}_{-0.13}$ (syst)

Table 5: Best fit values of A_0, A_4 and g^2_{LQ} for vector LQ models. Results are shown for a candidate m_{LQ} of 2.5 TeV.

Model	A_0	A_4	g^2_{LQ}
V_{eu}	0.05 ± 0.07	1.66 ± 0.08	$-0.09^{+0.03}_{-0.03}$ (stat)$^{+0.04}_{-0.08}$ (syst)
V_{ed}	0.06 ± 0.07	1.64 ± 0.08	$0.13^{+0.06}_{-0.06}$ (stat)$^{+0.17}_{-0.09}$ (syst)
$V_{\mu u}$	0.01 ± 0.05	1.63 ± 0.06	$-0.10^{+0.02}_{-0.02}$ (stat)$^{+0.04}_{-0.08}$ (syst)
$V_{\mu d}$	0.01 ± 0.05	1.61 ± 0.06	$0.14^{+0.05}_{-0.05}$ (stat)$^{+0.14}_{-0.07}$ (syst)

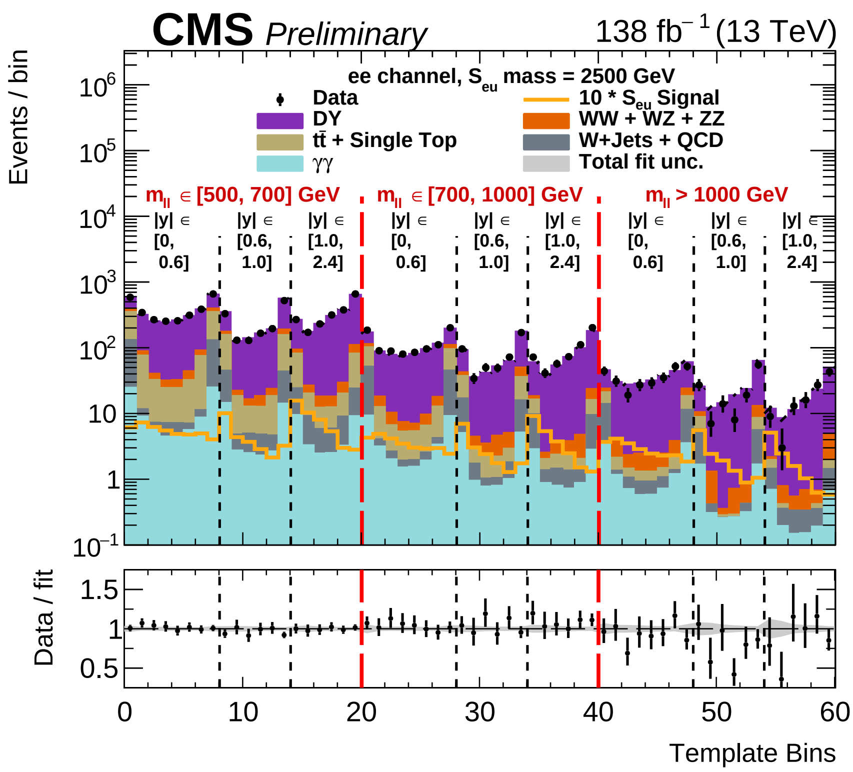

Figure 3: The observed data in the dielectron channel and the fitted signal-plus-background templates, shown for the S_{eu} scenario with a candidate LQ mass of 2.5 TeV. The black points are the observed data, the stacked histograms represent the backgrounds, and the yellow histogram shows the fitted LQ signal multiplied by 10. Distributions of events are binned in reconstructed $m_{\ell\ell}$, $|y|$ and c_R.

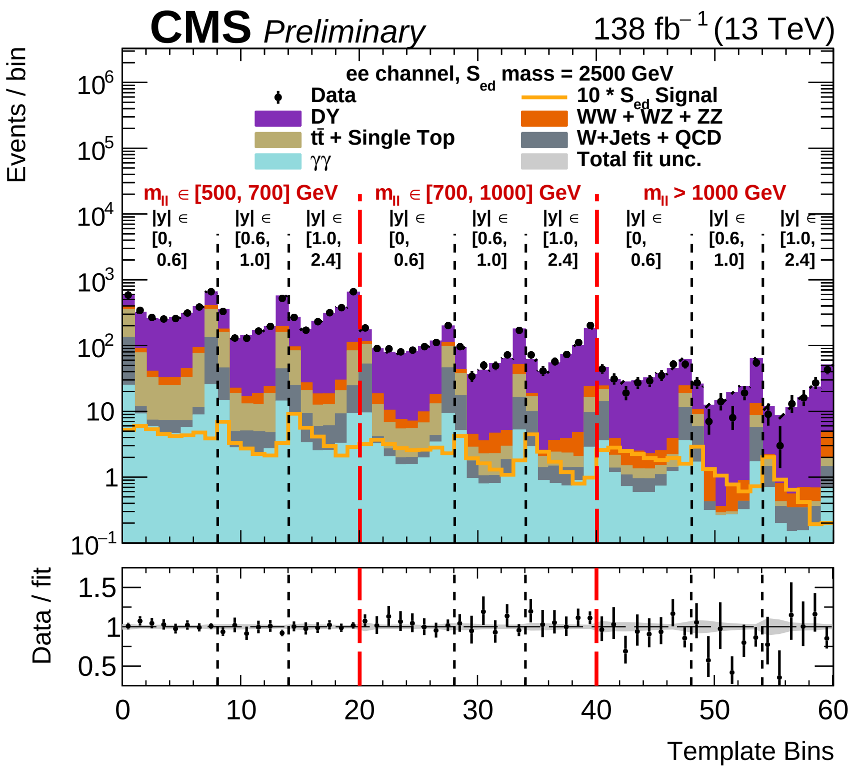

Figure 4: The observed data in the dielectron channel and the fitted signal-plus-background templates, shown for the S_{ed} scenario with a candidate LQ mass of 2.5 TeV. The black points are the observed data, the stacked histograms represent the backgrounds, and the yellow histogram shows the fitted LQ signal multiplied by 10. Distributions of events are binned in reconstructed $m_{\ell\ell}$, $|y|$ and c_R.

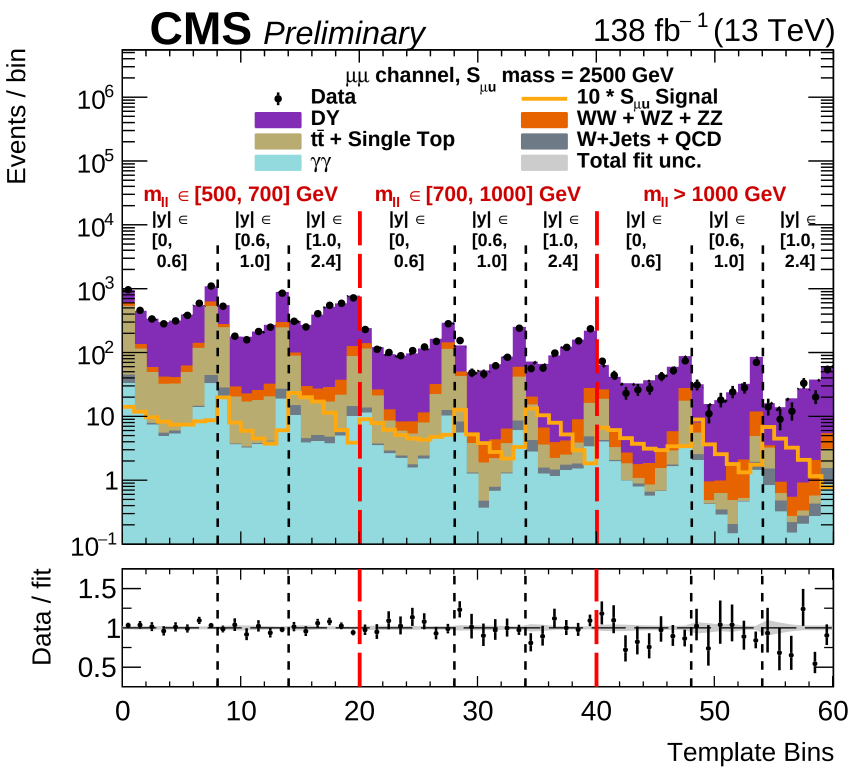

Figure 5: The observed data in the dimuon channel and the fitted signal-plus-background templates, shown for the $S_{\mu u}$ scenario with a candidate LQ mass of 2.5 TeV. The black points are the observed data, the stacked histograms represent the backgrounds, and the yellow histogram shows the fitted LQ signal multiplied by 10. Distributions of events are binned in reconstructed $m_{\ell\ell}$, $|y|$ and c_{R}.

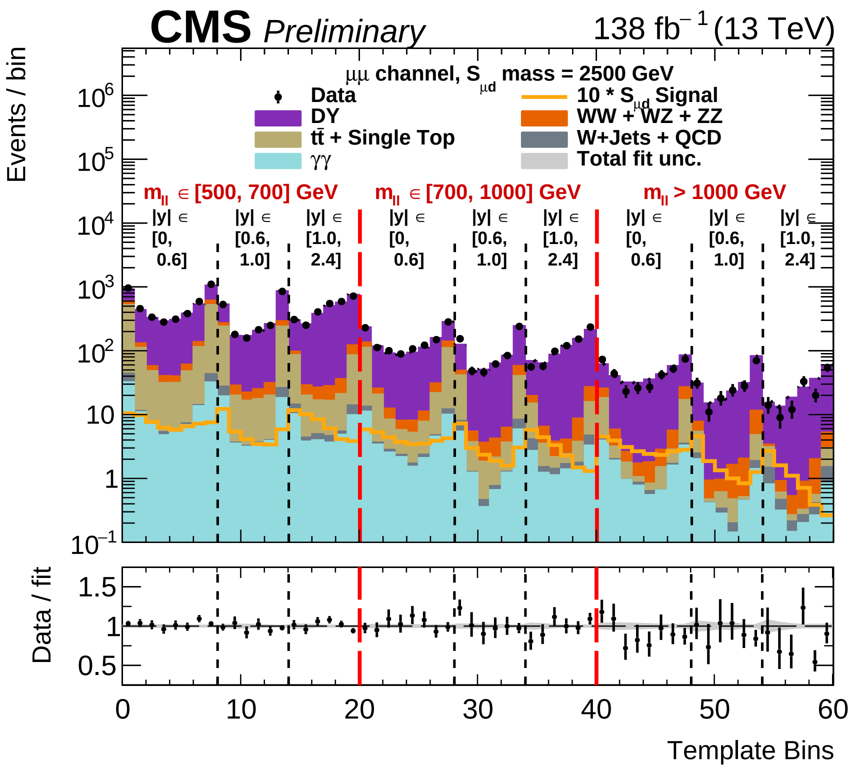

Figure 6: The observed data in the dimuon channel and the fitted signal-plus-background templates, shown for the $S_{\mu d}$ scenario with a candidate LQ mass of 2.5 TeV. The black points are the observed data, the stacked histograms represent the backgrounds, and the yellow histogram shows the fitted LQ signal multiplied by 10. Distributions of events are binned in reconstructed $m_{\ell\ell}$, $|y|$ and c_{R}.

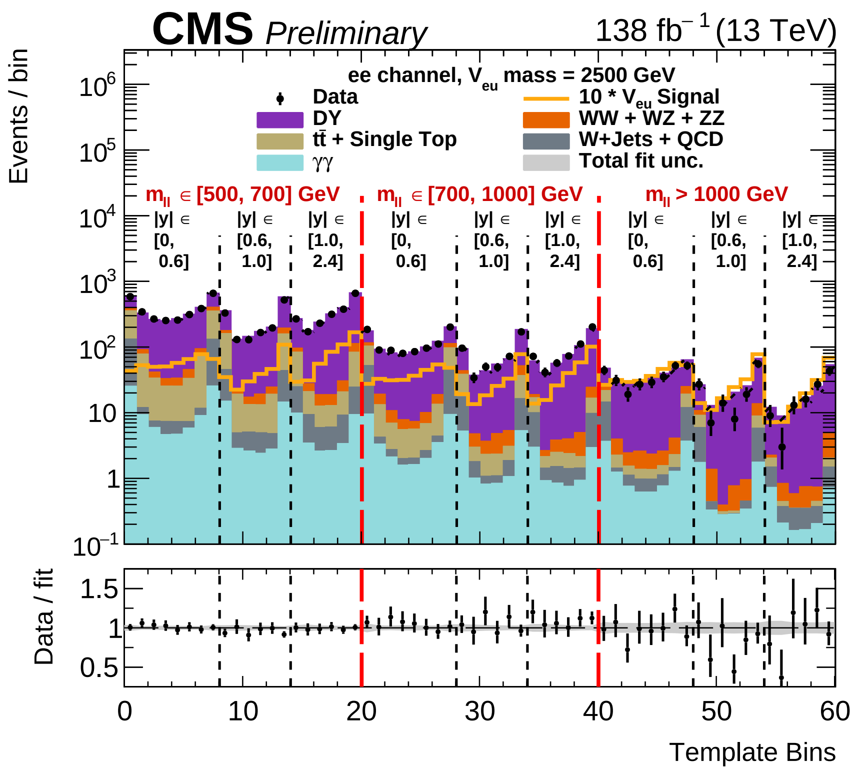

Figure 7: The observed data in the dielectron channel and the fitted signal-plus-background templates, shown for the V_{eu} scenario with a candidate LQ mass of 2.5 TeV. The black points are the observed data, the stacked histograms represent the backgrounds, and the yellow histogram shows the fitted LQ signal multiplied by 10. Distributions of events are binned in reconstructed $m_{\ell\ell}$, $|y|$ and c_{R}.

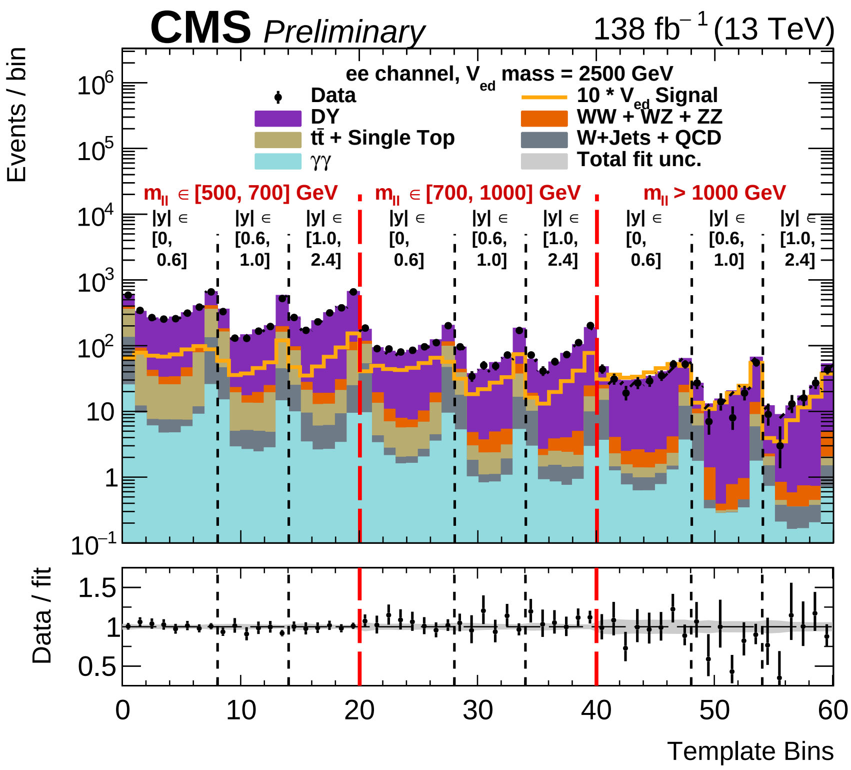

Figure 8: The observed data in the dielectron channel and the fitted signal-plus-background templates, shown for the V_{ed} scenario with a candidate LQ mass of 2.5 TeV. The black points are the observed data, the stacked histograms represent the backgrounds, and the yellow histogram shows the fitted LQ signal multiplied by 10. Distributions of events are binned in reconstructed $m_{\ell\ell}$, $|y|$ and c_{R}.

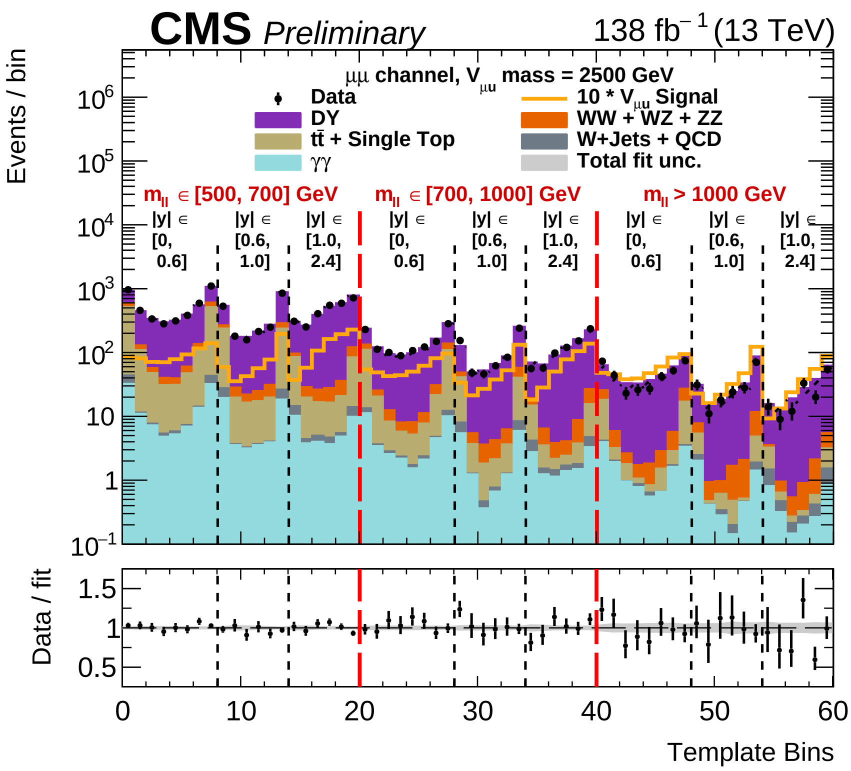

Figure 9: The observed data in the dimuon channel and the fitted signal-plus-background templates, shown for the $V_{\mu u}$ scenario with a candidate LQ mass of 2.5 TeV. The black points are the observed data, the stacked histograms represent the backgrounds, and the yellow histogram shows the fitted LQ signal multiplied by 10. Distributions of events are binned in reconstructed $m_{\ell\ell}$, $|y|$ and c_{R}.

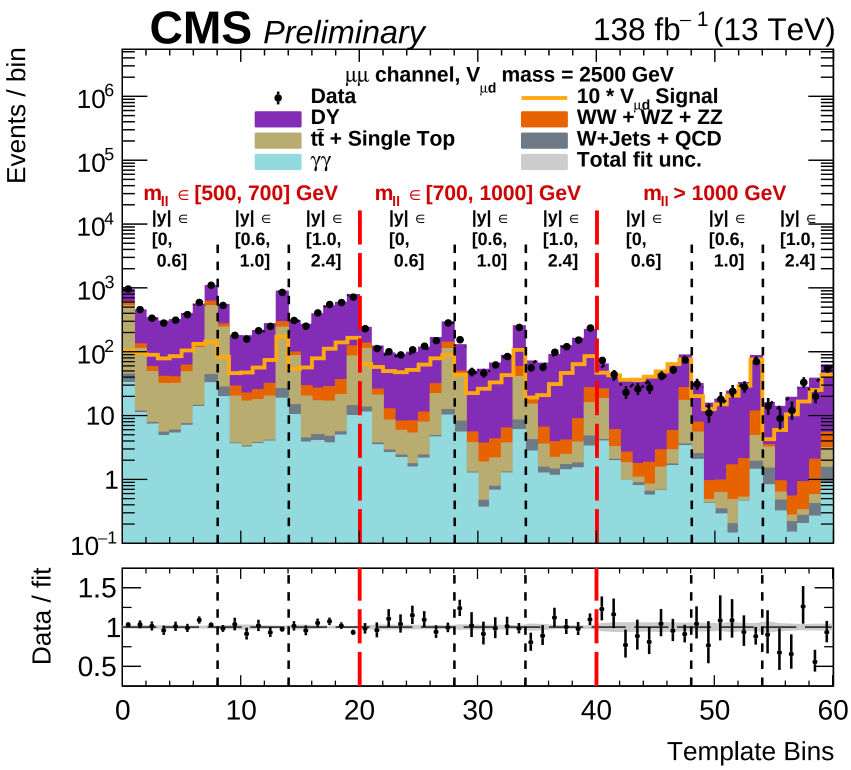

Figure 10: The observed data in the dimuon channel and the fitted signal-plus-background templates, shown for the $V_{\mu d}$ scenario with a candidate LQ mass of 2.5 TeV. The black points are the observed data, the stacked histograms represent the backgrounds, and the yellow histogram shows the fitted LQ signal multiplied by 10. Distributions of events are binned in reconstructed $m_{\ell\ell}$, $|y|$ and c_{R}.

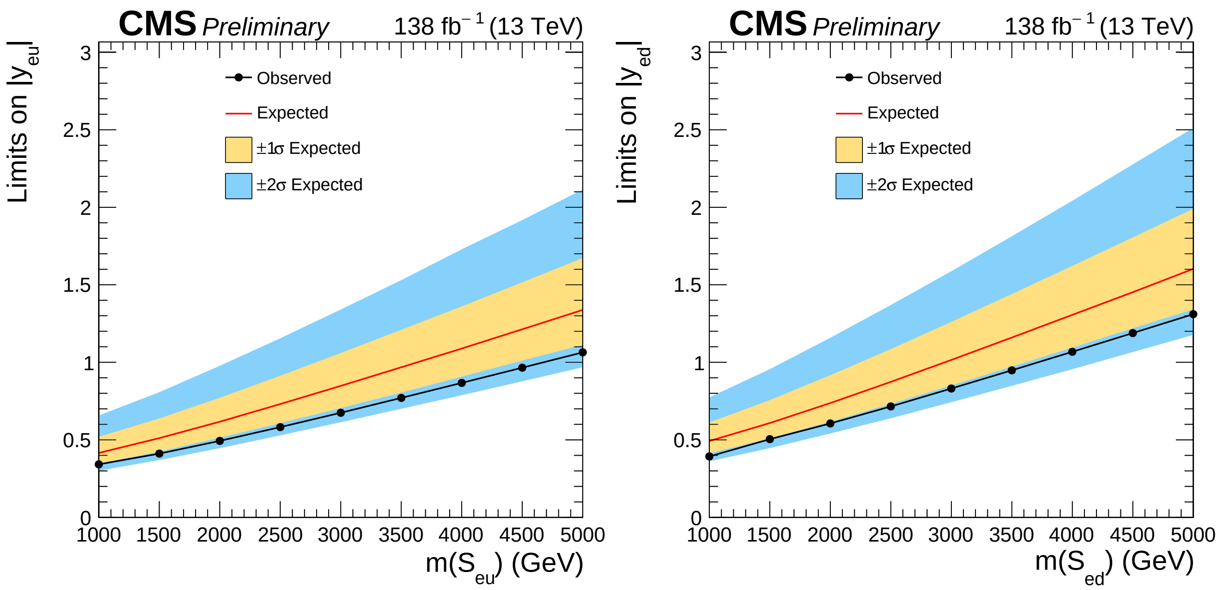

Figure 11: Upper limits at 95% CL on the LQ-fermion couplings, y_{eu} (left) and y_{ed} (right), versus m_{LQ} for scalar LQs coupling to electrons. The black points show the observed limits, the red line shows the expected limits, and the yellow and blue bands show the variations on the expected limit at the 1 and 2 standard deviation levels.

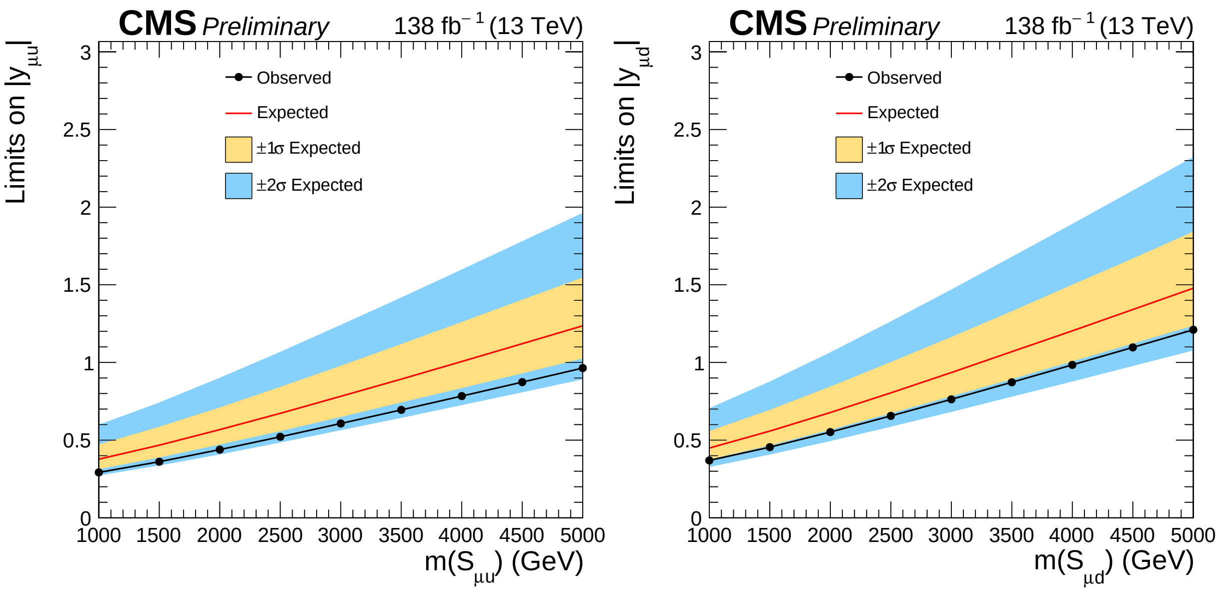

Figure 12: Upper limits at 95% CL on the LQ-fermion couplings, $y_{\mu \mathrm{u}}$ (left) and $y_{\mu \mathrm{d}}$ (right), versus m_{LQ} for scalar LQs coupling to muons. The black points show the observed limits, the red line shows the expected limits, and the yellow and blue bands show the variations on the expected limit at the 1 and 2 standard deviation levels.

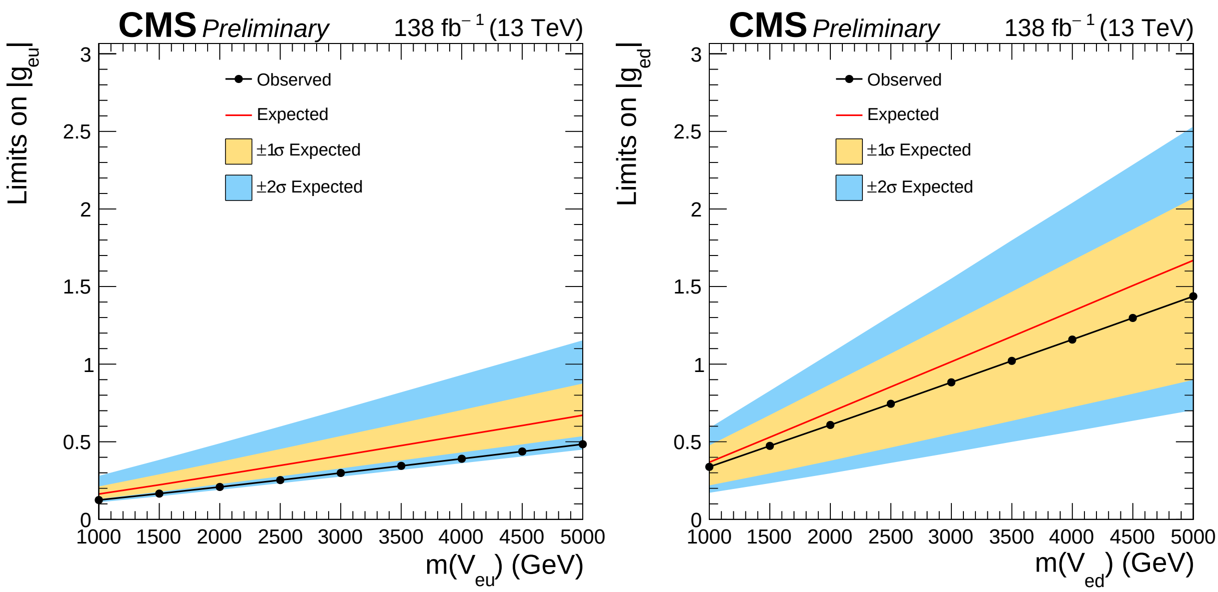

Figure 13: Upper limits at 95% CL on the LQ-fermion couplings, g_{eu} (left) and g_{ed} (right), versus m_{LQ} for vector LQs coupling to electrons. The black points show the observed limits, the red line shows the expected limits, and the yellow and blue bands show the variations on the expected limit at the 1 and 2 standard deviation levels.

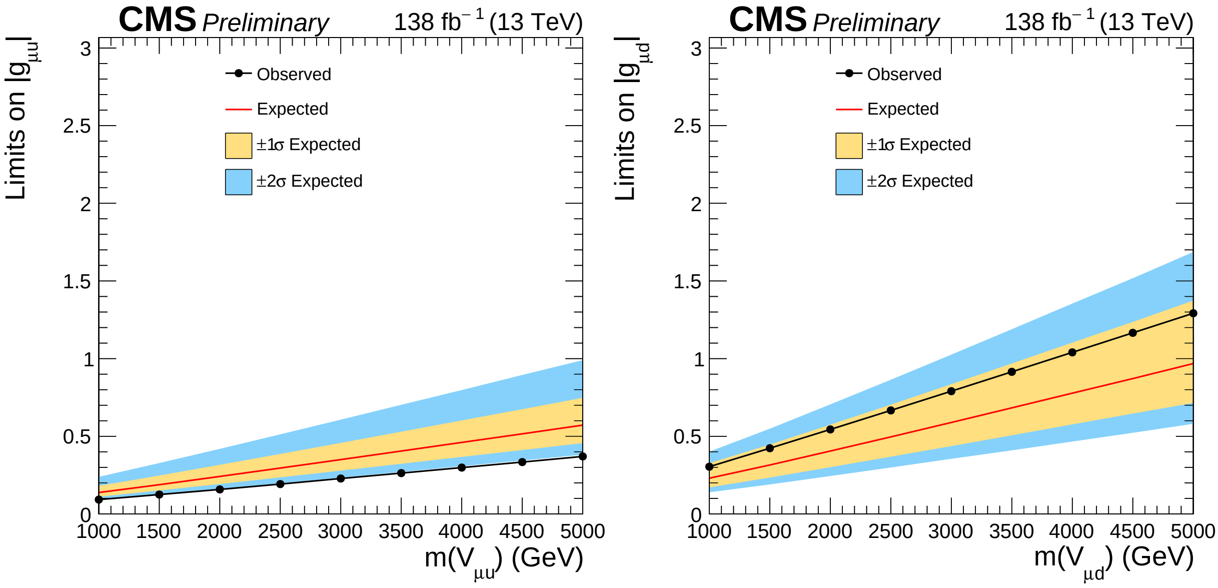

Figure 14: Upper limits at 95% CL on the LQ-fermion couplings, $g_{\mu\mathrm{u}}$ (left) and $g_{\mu\mathrm{d}}$ (right), versus m_{LQ} for vector LQs coupling to muons. The black points show the observed limits, the red line shows the expected limits, and the yellow and blue bands show the variations on the expected limit at the 1 and 2 standard deviation levels.

responding to an integrated luminosity of 138 fb^{-1}. Both scalar and vector LQ scenarios are considered, with masses between 1–5 TeV for exclusive LQ couplings to an up or a down quark and an electron or a muon. The t-channel exchange of a LQ modifies the dilepton angular distributions at masses well below the resonance mass of the LQ. A template fit to the angular and invariant mass distributions of high-mass dilepton events is used to distinguish the signal process from the dominant Drell–Yan background, incorporating interference effects. No evidence for such LQs is observed, and limits are set at 95% confidence level on the LQ-fermion couplings. Coupling values greater than 0.4–1.1 (0.3–1.0) are excluded for scalar LQs with masses from 1–5 TeV coupling to an electron (muon) and a first-generation quark. Similarly, for vector LQs, coupling values greater than 0.2–0.5 (0.1–0.4) are excluded. This search is sensitive to LQs with significantly higher masses than prior single- and pair-production searches, establishing the best limits on LQs with masses up to 5 TeV, and is also the first to set limits on vector LQs coupling to first- and second-generation fermions.

References

[1] J. C. Pati and A. Salam, “Lepton Number as the Fourth Color”, *Phys. Rev. D* **10** (1974) 275, doi:10.1103/PhysRevD.10.275. [Erratum: Phys.Rev.D 11, 703–703 (1975)].

[2] H. Georgi and S. L. Glashow, “Unity of all elementary particle forces”, *Phys. Rev. Lett.* **32** (1974) 438, doi:10.1103/PhysRevLett.32.438.

[3] S. Davidson and S. Descotes-Genon, “Minimal flavour violation for leptoquarks”, *JHEP* **11** (2010) 073, doi:10.1007/JHEP11(2010)073, arXiv:1009.1998.

[4] I. Dorsner and P. Fileviez Perez, “Unification without supersymmetry: Neutrino mass, proton decay and light leptoquarks”, *Nucl. Phys. B* **723** (2005) 53, doi:10.1016/j.nuclphysb.2005.06.016, arXiv:hep-ph/0504276.

[5] W. Buchmuller and D. Wyler, "Constraints on SU(5) type leptoquarks", *Phys. Lett. B* **177** (1986) 377, doi:10.1016/0370-2693(86)90771-9.

[6] B. Gripaios, M. Nardecchia, and S. A. Renner, "Composite leptoquarks and anomalies in *b*-meson decays", *JHEP* **05** (2015) 006, doi:10.1007/JHEP05(2015)006, arXiv:1412.1791.

[7] B. Gripaios, "Composite leptoquarks at the LHC", *JHEP* **02** (2010) 045, doi:10.1007/JHEP02(2010)045, arXiv:0910.1789.

[8] E. Farhi and L. Susskind, "Technicolor", *Phys. Rept.* **74** (1981) 277, doi:10.1016/0370-1573(81)90173-3.

[9] S. Dimopoulos, "Technicolored signatures", *Nucl. Phys. B* **168** (1980) 69, doi:10.1016/0550-3213(80)90277-1.

[10] B. Schrempp and F. Schrempp, "Light leptoquarks", *Phys. Lett. B* **153** (1985) 101, doi:10.1016/0370-2693(85)91450-9.

[11] M. J. Baker et al., "The coannihilation codex", *JHEP* **12** (2015) 120, doi:10.1007/JHEP12(2015)120, arXiv:1510.03434.

[12] S.-M. Choi, Y.-J. Kang, H. M. Lee, and T.-G. Ro, "Lepto-Quark portal dark matter", *JHEP* **10** (2018) 104, doi:10.1007/JHEP10(2018)104, arXiv:1807.06547.

[13] R. Barbier et al., "R-parity violating supersymmetry", *Phys. Rept.* **420** (2005) 1, doi:10.1016/j.physrep.2005.08.006, arXiv:hep-ph/0406039.

[14] Muon g-2 Collaboration, "Measurement of the positive muon anomalous magnetic moment to 0.46 ppm", *Phys. Rev. Lett.* **126** (2021), no. 14, 141801, doi:10.1103/PhysRevLett.126.141801, arXiv:2104.03281.

[15] S. Borsanyi et al., "Leading hadronic contribution to the muon magnetic moment from lattice QCD", *Nature* **593** (2021) 51, doi:10.1038/s41586-021-03418-1, arXiv:2002.12347.

[16] M. Du, J. Liang, Z. Liu, and V. Q. Tran, "A vector leptoquark interpretation of the muon $g-2$ and b anomalies", 2021. https://arxiv.org/abs/2104.05685.

[17] I. Doršner et al., "Physics of leptoquarks in precision experiments and at particle colliders", *Phys. Rept.* **641** (2016) 1, doi:10.1016/j.physrep.2016.06.001, arXiv:1603.04993.

[18] CMS Collaboration, "Search for a third-generation leptoquark coupled to a τ lepton and a b quark through single, pair, and nonresonant production in proton-proton collisions at $\sqrt{s} = 13$ TeV", *JHEP* **05** (2024) 311, doi:10.1007/JHEP05(2024)311, arXiv:2308.07826.

[19] CMS Collaboration, "Searches for additional Higgs bosons and for vector leptoquarks in $\tau\tau$ final states in proton-proton collisions at $\sqrt{s} = 13$ TeV", *JHEP* **07** (2023) 073, doi:10.1007/JHEP07(2023)073, arXiv:2208.02717.

[20] ATLAS Collaboration, "Search for pair production of third-generation leptoquarks decaying into a bottom quark and a τ-lepton with the ATLAS detector", *Eur. Phys. J. C* **83** (2023) 1075, doi:10.1140/epjc/s10052-023-12104-7, arXiv:2303.01294.

[21] ATLAS Collaboration, "Search for leptoquarks decaying into the bτ final state in pp collisions at $\sqrt{s}$ = 13 TeV with the ATLAS detector", *JHEP* **10** (2023) 001, doi:10.1007/JHEP10(2023)001, arXiv:2305.15962.

[22] ATLAS Collaboration, "Search for pairs of scalar leptoquarks decaying into quarks and electrons or muons in $\sqrt{s}$ = 13 TeV pp collisions with the ATLAS detector", *JHEP* **10** (2020) 112, doi:10.1007/JHEP10(2020)112, arXiv:2006.05872.

[23] CMS Collaboration, "Search for single production of scalar leptoquarks in proton-proton collisions at $\sqrt{s} = 8$ TeV", *Phys. Rev. D* **93** (2016) 032005, doi:10.1103/PhysRevD.93.032005, arXiv:1509.03750. [Erratum: Phys.Rev.D 95, 039906 (2017)].

[24] CMS Collaboration, "Search for pair production of first-generation scalar leptoquarks at $\sqrt{s} = 13$ TeV", *Phys. Rev. D* **99** (2019) 052002, doi:10.1103/PhysRevD.99.052002, arXiv:1811.01197.

[25] CMS Collaboration, "Search for pair production of second-generation leptoquarks at $\sqrt{s} = 13$ TeV", *Phys. Rev. D* **99** (2019) 032014, doi:10.1103/PhysRevD.99.032014, arXiv:1808.05082.

[26] N. Raj, "Anticipating nonresonant new physics in dilepton angular spectra at the LHC", *Phys. Rev. D* **95** (2017) 015011, doi:10.1103/PhysRevD.95.015011, arXiv:1610.03795.

[27] I. Bigaran and R. R. Volkas, "Getting chirality right: Single scalar leptoquark solutions to the $(g-2)_{e,\mu}$ puzzle", *Phys. Rev. D* **102** (2020) 075037, doi:10.1103/PhysRevD.102.075037, arXiv:2002.12544.

[28] D. Bečirević, N. Košnik, O. Sumensari, and R. Zukanovich Funchal, "Palatable leptoquark scenarios for lepton flavor violation in exclusive $b \to s\ell_1\ell_2$ modes", *JHEP* **11** (2016) 035, doi:10.1007/JHEP11(2016)035, arXiv:1608.07583.

[29] J. C. Collins and D. E. Soper, "Angular Distribution of Dileptons in High-Energy Hadron Collisions", *Phys. Rev. D* **16** (1977) 2219, doi:10.1103/PhysRevD.16.2219.

[30] CMS Collaboration, "Measurement of the Drell-Yan forward-backward asymmetry at high dilepton masses in proton-proton collisions at $\sqrt{s}$ = 13 TeV", *JHEP* **2022** (2022) 063, doi:10.1007/JHEP08(2022)063, arXiv:2202.12327.

[31] E. Mirkes, "Angular decay distribution of leptons from W bosons at NLO in hadronic collisions", *Nucl. Phys. B* **387** (1992) 3, doi:10.1016/0550-3213(92)90046-E.

[32] E. Mirkes and J. Ohnemus, "Angular distributions of Drell-Yan lepton pairs at the Tevatron: Order $\alpha - s^2$ corrections and Monte Carlo studies", *Phys. Rev. D* **51** (1995) 4891, doi:10.1103/PhysRevD.51.4891, arXiv:hep-ph/9412289.

[33] CMS Collaboration, "The CMS experiment at the CERN LHC", *JINST* **3** (2008) S08004, doi:10.1088/1748-0221/3/08/S08004.

[34] CMS Collaboration, "Development of the CMS detector for the CERN LHC Run 3", *JINST* **19** (2024) P05064, doi:10.1088/1748-0221/19/05/P05064, arXiv:2309.05466.

[35] CMS Collaboration, "Performance of the CMS Level-1 trigger in proton-proton collisions at $\sqrt{s} = 13\,\text{TeV}$", *JINST* **15** (2020) P10017, doi:10.1088/1748-0221/15/10/P10017, arXiv:2006.10165.

[36] CMS Collaboration, "The CMS trigger system", *JINST* **12** (2017) P01020, doi:10.1088/1748-0221/12/01/P01020, arXiv:1609.02366.

[37] CMS Collaboration, "Particle-flow reconstruction and global event description with the CMS detector", *JINST* **12** (2017) P10003, doi:10.1088/1748-0221/12/10/P10003, arXiv:1706.04965.

[38] CMS Collaboration, "Technical proposal for the Phase-II upgrade of the Compact Muon Solenoid", CMS Technical Proposal CERN-LHCC-2015-010, CMS-TDR-15-02, 2015.

[39] CMS Collaboration, "Performance of the CMS muon detector and muon reconstruction with proton-proton collisions at $\sqrt{s} = 13$ TeV", *JINST* **13** (2018) P06015, doi:10.1088/1748-0221/13/06/P06015, arXiv:1804.04528.

[40] CMS Collaboration, "Electron and photon reconstruction and identification with the CMS experiment at the CERN LHC", *JINST* **16** (2021) P05014, doi:10.1088/1748-0221/16/05/P05014, arXiv:2012.06888.

[41] M. Cacciari, G. P. Salam, and G. Soyez, "The anti-k_{T} jet clustering algorithm", *JHEP* **04** (2008) 063, doi:10.1088/1126-6708/2008/04/063, arXiv:0802.1189.

[42] M. Cacciari, G. P. Salam, and G. Soyez, "FastJet user manual", *Eur. Phys. J. C* **72** (2012) 1896, doi:10.1140/epjc/s10052-012-1896-2, arXiv:1111.6097.

[43] CMS Collaboration, "Pileup mitigation at CMS in 13 TeV data", *JINST* **15** (2020) P09018, doi:10.1088/1748-0221/15/09/p09018, arXiv:2003.00503.

[44] CMS Collaboration, "Jet energy scale and resolution in the CMS experiment in pp collisions at 8 TeV", *JINST* **12** (2017) P02014, doi:10.1088/1748-0221/12/02/P02014, arXiv:1607.03663.

[45] CMS Collaboration, "Performance of missing transverse momentum reconstruction in proton-proton collisions at $\sqrt{s} = 13\,\text{TeV}$ using the CMS detector", *JINST* **14** (2019) P07004, doi:10.1088/1748-0221/14/07/P07004, arXiv:1903.06078.

[46] J. Alwall et al., "The automated computation of tree-level and next-to-leading order differential cross sections, and their matching to parton shower simulations", *JHEP* **07** (2014) 079, doi:10.1007/JHEP07(2014)079, arXiv:1405.0301.

[47] T. Sjöstrand et al., "An introduction to PYTHIA 8.2", *Comput. Phys. Commun.* **191** (2015) 159, doi:10.1016/j.cpc.2015.01.024, arXiv:1410.3012.

[48] R. D. Ball et al., "A first unbiased global NLO determination of parton distributions and their uncertainties", *Nucl. Phys. B* **838** (2010) 136, doi:10.1016/j.nuclphysb.2010.05.008, arXiv:1002.4407.

[49] NNPDF Collaboration, "Parton distributions for the LHC Run II", *JHEP* **04** (2015) 040, doi:10.1007/JHEP04(2015)040, arXiv:1410.8849.

[50] P. Nason, "A new method for combining NLO QCD with shower Monte Carlo algorithms", *JHEP* **11** (2004) 040, doi:10.1088/1126-6708/2004/11/040, arXiv:hep-ph/0409146.

[51] S. Frixione, P. Nason, and C. Oleari, "Matching NLO QCD computations with parton shower simulations: the POWHEG method", *JHEP* **11** (2007) 070, doi:10.1088/1126-6708/2007/11/070, arXiv:0709.2092.

[52] S. Alioli, P. Nason, C. Oleari, and E. Re, "A general framework for implementing NLO calculations in shower Monte Carlo programs: the POWHEG BOX", *JHEP* **06** (2010) 043, doi:10.1007/JHEP06(2010)043, arXiv:1002.2581.

[53] S. Frixione, P. Nason, and G. Ridolfi, "A positive-weight next-to-leading-order Monte Carlo for heavy flavour hadroproduction", *JHEP* **09** (2007) 126, doi:10.1088/1126-6708/2007/09/126, arXiv:0707.3088.

[54] CMS Collaboration, "Investigations of the impact of the parton shower tuning in Pythia 8 in the modelling of $\mathrm{t\bar{t}}$ at $\sqrt{s} = 8$ and 13 TeV", Physics Analysis Summary CMS-PAS-TOP-16-021, 2016.

[55] L. Forthomme, "CepGen – A generic central exclusive processes event generator for hadron-hadron collisions", *Comput. Phys. Commun.* **271** (2022) 108225, doi:10.1016/j.cpc.2021.108225, arXiv:1808.06059.

[56] J. A. M. Vermaseren, "Two photon processes at very high-energies", *Nucl. Phys. B* **229** (1983) 347, doi:10.1016/0550-3213(83)90336-X.

[57] S. Baranov, O. Düenger, H. Shooshtari, and J. Vermaseren, "LPAIR: A generator for lepton pair production", in *Workshop on Physics at HERA*, p. 1478. 1991.

[58] T. Sjöstrand, S. Mrenna, and P. Z. Skands, "PYTHIA 6.4 physics and manual", *JHEP* **05** (2006) 026, doi:10.1088/1126-6708/2006/05/026, arXiv:hep-ph/0603175.

[59] A. Suri and D. R. Yennie, "The space-time phenomenology of photon absorbtion and inelastic electron scattering", *Annals Phys.* **72** (1972) 243, doi:10.1016/0003-4916(72)90242-4.

[60] J. M. Campbell, R. K. Ellis, and W. T. Giele, "A multi-threaded version of MCFM", *Eur. Phys. J. C* **75** (2015) 246, doi:10.1140/epjc/s10052-015-3461-2, arXiv:1503.06182.

[61] T. Gehrmann et al., "W^+W^- production at hadron colliders in next to next to leading order QCD", *Phys. Rev. Lett.* **113** (2014) 212001, doi:10.1103/PhysRevLett.113.212001, arXiv:1408.5243.

[62] M. Czakon and A. Mitov, "Top++: A program for the calculation of the top-pair cross-section at hadron colliders", *Comput. Phys. Commun.* **185** (2014) 2930, doi:10.1016/j.cpc.2014.06.021, arXiv:1112.5675.

[63] A. Crivellin and L. Schnell, "Complete Lagrangian and set of Feynman rules for scalar leptoquarks", *Comput. Phys. Commun.* **271** (2022) 108188, doi:10.1016/j.cpc.2021.108188, arXiv:2105.04844.

[64] GEANT4 Collaboration, "GEANT4–a simulation toolkit", *Nucl. Instrum. Meth. A* **506** (2003) 250, doi:10.1016/S0168-9002(03)01368-8.

[65] CMS Collaboration, "Performance of the reconstruction and identification of high-momentum muons in proton-proton collisions at $\sqrt{s} = 13$ TeV", *JINST* **15** (2020) P02027, doi:10.1088/1748-0221/15/02/P02027, arXiv:1912.03516.

[66] Y. Afik et al., "High p_t correlated tests of lepton universality in lepton(s) + jet(s) processes; an EFT analysis", *Phys. Lett. B* **811** (2020) 135908, doi:10.1016/j.physletb.2020.135908, arXiv:2005.06457.

[67] CMS Collaboration, "Measurement of the differential Drell-Yan cross section in proton-proton collisions at $\sqrt{s} = 13$ TeV", *JHEP* **12** (2019) 059, doi:10.1007/JHEP12(2019)059, arXiv:1812.10529.

[68] CMS Collaboration, "Search for physics beyond the standard model in dilepton mass spectra in proton-proton collisions at $\sqrt{s} = 8$ TeV", *JHEP* **04** (2015) 025, doi:10.1007/JHEP04(2015)025, arXiv:1412.6302.

[69] Particle Data Group, P. A. Zyla et al., "Review of particle physics", *Prog. Theor. Exp. Phys.* **2020** (2020) 083C01, doi:10.1093/ptep/ptaa104.

[70] CMS Collaboration, "Measurement of the top quark forward-backward production asymmetry and the anomalous chromoelectric and chromomagnetic moments in pp collisions at $\sqrt{s} = 13$ TeV", *JHEP* **06** (2020) 146, doi:10.1007/JHEP06(2020)146, arXiv:1912.09540.

[71] A. Manohar, P. Nason, G. P. Salam, and G. Zanderighi, "How bright is the proton? A precise determination of the photon parton distribution function", *Phys. Rev. Lett.* **117** (2016) 242002, doi:10.1103/PhysRevLett.117.242002, arXiv:1607.04266.

[72] A. V. Manohar, P. Nason, G. P. Salam, and G. Zanderighi, "The photon content of the proton", *JHEP* **12** (2017) 046, doi:10.1007/JHEP12(2017)046, arXiv:1708.01256.

[73] J. S. Conway, "Incorporating Nuisance Parameters in Likelihoods for Multisource Spectra", in *PHYSTAT 2011*, p. 115. 2011. arXiv:1103.0354. doi:10.5170/CERN-2011-006.115.

[74] CMS Collaboration, "Precision luminosity measurement in proton-proton collisions at $\sqrt{s} = 13$ TeV in 2015 and 2016 at CMS", *Eur. Phys. J. C* **81** (2021) 800, doi:10.1140/epjc/s10052-021-09538-2, arXiv:2104.01927.

[75] CMS Collaboration, "CMS luminosity measurement for the 2017 data-taking period at $\sqrt{s} = 13$ TeV", CMS Physics Analysis Summary CMS-PAS-LUM-17-004, 2018.

[76] CMS Collaboration, "CMS luminosity measurement for the 2018 data-taking period at $\sqrt{s} = 13$ TeV", CMS Physics Analysis Summary CMS-PAS-LUM-18-002, 2019.

[77] CMS Collaboration, "The CMS statistical analysis and combination tool: COMBINE", 2024. arXiv:2404.06614. Submitted to *Comput. Softw. Big Sci.*

[78] A. L. Read, "Presentation of search results: The $\mathrm{CL_s}$ technique", *J. Phys. G* **28** (2002) 2693, doi:10.1088/0954-3899/28/10/313.

[79] T. Junk, "Confidence level computation for combining searches with small statistics", *Nucl. Instrum. Meth. A* **434** (1999) 435, doi:10.1016/S0168-9002(99)00498-2, arXiv:hep-ex/9902006.

[80] G. Cowan, K. Cranmer, E. Gross, and O. Vitells, "Asymptotic formulae for likelihood-based tests of new physics", *Eur. Phys. J. C* **71** (2011) 1554, doi:10.1140/epjc/s10052-011-1554-0, arXiv:1007.1727. [Erratum: Eur.Phys.J.C 73, 2501 (2013)].